

See discussions, stats, and author profiles for this publication at: <https://www.researchgate.net/publication/26720540>

# Energy Gaps in the $4f(13)5d(1)$ Manifold and Multiple Spontaneous Emissions in $\text{Yb}^{2+}$ -Doped $\text{CsCaBr}_3$

ARTICLE *in* THE JOURNAL OF PHYSICAL CHEMISTRY A · AUGUST 2009

Impact Factor: 2.69 · DOI: 10.1021/jp904868b · Source: PubMed

---

CITATIONS

13

---

READS

52

3 AUTHORS, INCLUDING:



Goar Sánchez

University College Dublin

69 PUBLICATIONS 900 CITATIONS

SEE PROFILE



Luis Seijo

Universidad Autónoma de Madrid

160 PUBLICATIONS 3,801 CITATIONS

SEE PROFILE

# Energy Gaps in the $4f^{13}5d^1$ Manifold and Multiple Spontaneous Emissions in $\text{Yb}^{2+}$ -Doped $\text{CsCaBr}_3$ <sup>†</sup>

Goar Sánchez-Sanz,<sup>‡</sup> Luis Seijo,<sup>‡,§</sup> and Zoila Barandiarán<sup>\*,‡,§</sup>

Departamento de Química, C-XIV, Universidad Autónoma de Madrid, 28049 Madrid, Spain, and Instituto Universitario de Ciencia de Materiales Nicolás Cabrera, Universidad Autónoma de Madrid, 28049 Madrid, Spain

Received: May 25, 2009; Revised Manuscript Received: July 14, 2009

Multiple spontaneous  $4f^{13}5d^1 \rightarrow 4f^{14}$  emissions are predicted in  $\text{Yb}^{2+}$ -doped  $\text{CsCaBr}_3$  crystals by ab initio quantum chemical calculations. Four emission bands are found at 23 900, 26 600, 34 600, and 43 900  $\text{cm}^{-1}$  that should be experimentally observable at low temperatures. The first, third, and fourth bands are slow, electric dipole forbidden emissions that can be described as spin-forbidden. The second band is a fast, electric dipole-allowed emission that cannot be described as spin-allowed, but as spin-enabled; its radiative emission lifetime is 400 ns. Large energy gaps (23 900, 4600, 4000  $\text{cm}^{-1}$ , respectively), relative to the maximum local phonon energies calculated (around 185  $\text{cm}^{-1}$ ), are found below the emitting levels of the slow bands, which indicates that these states should be significantly stable and multiphonon relaxation to the lower states should be negligible. A smaller gap (2600  $\text{cm}^{-1}$ ) separates the states of the fast band, which should result in a temperature dependent competition between radiative and nonradiative decay. Differential correlation between  $4f-4f$  and  $4f-5d$  pairs, splitting of the  $5d$  shell by interactions with the host, and spin-orbit effects within the  $4f^{13}$  subshell, are found to be responsible for the existence of the gaps, which, in turn, split the absorption spectrum into four groups of separate bands, three of which could lie below the host absorption threshold. The quantum chemical methods employed make use of explicit wave functions expanded in terms of flexible basis sets, multiconfigurational self-consistent-field and multireference second-order perturbation methods to account for nondynamic and dynamic electron correlation, scalar and relativistic terms in the  $(\text{YbBr}_6)^{4-}$  defect cluster Hamiltonian, and quantum mechanical embedding potentials to represent the host crystal.

## I. Introduction

Two characteristics of divalent lanthanide ions ( $\text{Ln}^{2+}$ ) in crystals can be pointed out as responsible for the growing number of reports on their optical properties in the past few years (see ref 1 for a review; for an overview on recent works see ref 2). First, their  $4f^N \rightarrow 4f^{N-1}5d^1$  excitations occur at much lower energies than in the isoelectronic trivalent series ( $\text{Ln}^{3+}$ ), in the near-IR, visible, and near-UV. As a consequence of this, large portions of their  $4f^{N-1}5d^1$  manifolds are experimentally accessible and a variety of crystals, including crystals of heavy (polarizable) halides, can be chosen as host matrices, in contrast with the wide band gap hosts (commonly fluorides and oxides) typically needed to reach the  $4f^{N-1}5d^1$  states in the  $\text{Ln}^{3+}$  series. Second, and very interesting from practical and basic points of view, the  $4f^{N-1}5d^1$  manifolds of the heavy members ( $N > 7$ ) may contain a number of metastable excited states, as deduced from the facts that two emission bands<sup>2,3</sup> and very unusual multiple spontaneous emissions<sup>3–5</sup> have been detected, and upconversion luminescence has been proven and interpreted in terms of energy transfer mechanisms where more than one  $4f^{N-1}5d^1$  state is involved.<sup>6,7</sup> These spectral features highlight the potentiality of divalent lanthanides in the fields of solid state lasers<sup>8</sup> and solid state lighting and show them as very promising phosphors for future technology based in their combination with light-emitting diodes as pump sources.<sup>6</sup> They also highlight the importance of providing ab initio theoretical descriptions to the

underlying electronic structures, for which semiquantitative models and schematic energy diagrams<sup>9</sup> or empirical crystal field analyses<sup>2</sup> are often used.

The stability of excited states of rare-earth ions in crystals was already investigated in very early spectroscopic works where it was observed that, if two spin-orbit levels were sufficiently close in energy, the upper level would not be sufficiently stable to fluoresce, a fact that promoted theoretical and experimental approaches to understanding multiphonon relaxation processes and their interplay with radiative processes (see refs 10–12 and references therein). As a consequence, a number of factors are now recognized to play an important role in favoring the stability of excited states.<sup>10–14</sup> Among them, a key factor is the existence of large energy gaps in the manifold of excited states, but also important are the value of the maximum phonon energy of the material and the spin character of the excited states separated by the gaps.<sup>10–14</sup>

The progress of solid state quantum chemical methods has made it possible to obtain information about these factors independently from experiments, this being the main characteristic of the so-called ab initio methods. The calculation of potential energy surfaces of excited states is a typical target for ab initio methods of quantum chemistry based on the explicit use of multiconfigurational wave functions.<sup>15–17</sup> When these methods are combined with embedding techniques<sup>18,19</sup> and the Hamiltonians used include scalar and spin-dependent relativistic terms,<sup>18,20</sup> they can be applied to the calculation of local excited states of f-elements in the solid state and to their phosphor properties.<sup>21–23</sup> From the analyses of the potential energy surfaces and the corresponding wave functions, the energy gaps

<sup>†</sup> Part of the “Russell M. Pitzer Festschrift”.

<sup>\*</sup> Corresponding author. Electronic address: zoila.barandiaran@uam.es.

<sup>‡</sup> Departamento de Química.

<sup>§</sup> Instituto Universitario de Ciencia de Materiales Nicolás Cabrera.

below excited states can be quantified, the energy of the local vibrational frequencies can be calculated, and the contributions of terms of different spin and spatial symmetries can be traced back from the spin–orbit wave functions. All of these results give the quantum chemical picture of existing empirical data on f-element based phosphors or the quantum chemical prediction of their luminescence data not yet available. In any case, the insight gained from the analyses of experiments using semiquantitative models or empirical theories, in these types of materials, is expanded.

In this work we have applied *ab initio* quantum chemical methods to the calculation of the energy gaps in the manifold of excited states of Yb<sup>2+</sup> doped CsCaBr<sub>3</sub> crystals to explore whether multiple spontaneous emissions can be expected in this material. The choice of this particular impurity–host combination also responds to the following reasons: (i) Yb<sup>2+</sup> is a good candidate among the heavy divalent lanthanides because it has the simplest possible 4f<sup>N</sup> manifold, formed by its spin-singlet 4f<sup>14</sup> ground state, which focuses the computational effort and analyses on the 4f<sup>N-1</sup>5d<sup>1</sup> and 4f<sup>N-1</sup>6s<sup>1</sup> excited manifolds, (ii) CsCaBr<sub>3</sub> is a good host because it has been recently shown to favor multiple emissions in heavy Ln<sup>2+</sup> ions like Tm<sup>2+</sup>,<sup>4</sup> and it is known that divalent lanthanides can be stabilized in this matrix,<sup>3,4,7</sup> (iii) as far as we know, the only report on the spectral features of CsCaBr<sub>3</sub>:Yb<sup>2+</sup> crystals is that of ref 3, where the 77 and 300 K emission spectra were presented in the range of 21 000 to 25 800 cm<sup>-1</sup> without any report on emission lifetime values, and, hence, the predictions of the present work should serve to evaluate the interest of and orient future experimental work on this material.

## II. Details of the Calculations

The quantum chemical methods employed here make use of explicit wave functions expanded in terms of flexible basis sets, multiconfigurational self-consistent-field<sup>15</sup> and multireference second-order perturbation methods<sup>16,17,24,25</sup> to account for non-dynamic and dynamic electron correlation, scalar and relativistic terms in the (YbBr<sub>6</sub>)<sup>4-</sup> defect cluster Hamiltonian,<sup>18,26</sup> and quantum mechanical embedding potentials to represent the host crystal.<sup>18,27</sup> All the methods used have been described elsewhere; therefore, we only give here the details necessary so that the present calculations are reproducible.

Within the (YbBr<sub>6</sub>)<sup>4-</sup> octahedral defect cluster, relativistic core *ab initio* model potentials (AIMP) have been used to represent the [Kr] core of Yb<sup>28</sup> and the [Ar, 3d] cores of Br;<sup>29</sup> the corresponding Yb valence basis set (14s10p10d8f),<sup>30</sup> supplemented with three g-type functions that give maximum radial overlap with the 4f atomic orbital, is contracted as [6s5p6d4f1g]; the Br basis set used, (9s9p4d)[3s5p2d], includes three d-type orthogonality functions that give maximum radial overlap with the 3d core orbital, one d-type polarization function<sup>31</sup> and one p-type diffuse function for anions with orbital exponent  $\zeta = 0.036\,816\,05$ .<sup>32</sup> We have also used a (10s7p)/[1s1p] basis set at the second neighbor Ca sites to favor strong orthogonality with the environment; the contracted Gaussian functions are the external Ca<sup>2+</sup> 3s and 3p embedded atomic orbitals calculated in the procedure followed to produce the AIMP embedding. The (YbBr<sub>6</sub>)<sup>4-</sup> Hamiltonian includes the AIMP embedding potentials obtained in a previous work<sup>33</sup> to represent the Cs<sup>+</sup>, Ca<sup>2+</sup>, and Br<sup>-</sup> ions located at their cubic crystal structure sites.<sup>34</sup> All the ions located within a cube of length 4a<sub>0</sub>, centered at the impurity site, have been represented by AIMP; point charges have been used for the rest of ions located within a cube of length 7a<sub>0</sub>; fractional charges have been

assigned to those located at the faces, edges, or corners of the outermost cube, following Evjen's method.<sup>35</sup>

Electron correlation and spin–orbit coupling have been combined together following a two-step method. In a first step, spin–orbit terms have been excluded in the embedded cluster Hamiltonian and state-average complete active space self-consistent field calculations (SA-CASSCF)<sup>15</sup> have been performed using the scalar terms of the relativistic Wood–Boring AIMP<sup>26</sup> Hamiltonian. The active space used results from distributing the 14 open-shell electrons in 13 active molecular orbitals with main character Yb 4f, 5d, 6s, this being the standard choice for a lanthanide.<sup>36</sup> These calculations are referred to as CASSCF(4f,5d,6s) in the next sections. Dynamic electron correlation has been taken into account using the SA-CASSCF wave functions in subsequent multistate second-order perturbation theory calculations (MS-CASPT2),<sup>16,17,24,25</sup> where 80 valence electrons occupying the cluster molecular orbitals with main character Br 4s, 4p and Yb 4d, 5s, 5p, 4f, and 5d/6s were correlated; these calculations are referred to as MS-CASPT2(Br48,Yb32). The program MOLCAS has been used for these calculations.<sup>37</sup> In a second step, the full Wood–Boring AIMP Hamiltonian,<sup>26</sup> which includes the spin–orbit coupling operator (scaled by a factor of 0.9, as proposed in ref 38), has been used to perform double-group spin–orbit configuration–interaction (CI) calculations. The shifting operator included in this Hamiltonian, the so-called spin-free-state-shifting (sfss) operator,<sup>39</sup> transports the dynamic electron correlation effects retrieved at the spin–orbit free MS-CASPT2(Br48,Yb32) level onto the smaller configurational space used in the spin–orbit CI calculations, which include the restricted active space formed by the 4f<sup>13</sup>5d<sup>1</sup> and 4f<sup>13</sup>6s<sup>1</sup> multireference plus all single excitations from the 4f, 5d, and 6s molecular orbitals to the virtual orbitals. For these calculations, the bases described above were truncated to Yb[6s5p6d4f], Br[3s3p]. We refer to these calculations as SO–CI; they have been done using the COLUMBUS package.<sup>40</sup> The EPCISO program<sup>41</sup> has been used to calculate electric dipole transition moments. All AIMP data (for embedding and/or for cores) and valence basis sets can be found in ref 42.

## III. Results and Discussion

We discuss here the results of a quantum chemical investigation of the absorption and luminescence properties of CsCaBr<sub>3</sub>:Yb<sup>2+</sup> to explore whether multiple spontaneous emissions can be expected in this material.

In a first subsection, the calculated electronic structure of the 4f<sup>13</sup>5d<sup>1</sup> and 4f<sup>13</sup>6s<sup>1</sup> states is described in detail and the origin of the energy gaps found in these manifolds is revealed. The lowest energy 4f<sup>13</sup>5d<sup>1</sup> states, namely, the 4f<sup>13</sup>5d(t<sub>2g</sub>)<sup>1</sup> states, where calculated in a previous work<sup>33</sup> in the context of a quantum chemical analysis of their high- and low-spin character which could reveal the spin-forbidden and spin-allowed nature of the lowest absorption bands of the CsCaBr<sub>3</sub>:Yb<sup>2+</sup> material; these results are used and summarized here, and are combined together with the results of the higher lying 4f<sup>13</sup>5d(e<sub>g</sub>)<sup>1</sup> and 4f<sup>13</sup>6s<sup>1</sup> states, as explained below. The structure of the whole absorption spectrum of CsCaBr<sub>3</sub>:Yb<sup>2+</sup> in separated groups of bands and their relative intensities are discussed in a second subsection. In a third subsection, a prediction is made, from theory alone, of which excited states should be stable enough to luminesce. Finally, in the last subsection the results of the calculation are confronted with available experimental information.

**A. Structure of the 4f<sup>13</sup>5d<sup>1</sup> and 4f<sup>13</sup>6s<sup>1</sup> Manifolds. Origin of the Energy Gaps.** The results of the calculations performed in the (YbBr<sub>6</sub>)<sup>4-</sup> defect cluster, embedded in the CsCaBr<sub>3</sub> host,

**TABLE 1: Results of the Calculations on the (YbBr<sub>6</sub>)<sup>4-</sup> Cluster That Include CsCaBr<sub>3</sub> Embedding, 80 Valence Electron Correlation, and Scalar Relativistic Effects<sup>a</sup>**

state	CASSCF(4f,5d,6s)			MS-CASPT2(Br48,Yb32)		
	$R_e$	$\bar{\nu}_{a_{1g}}$	$T_e$	$R_e$	$\bar{\nu}_{a_{1g}}$	$T_e$
1 <sup>1</sup> A <sub>1g</sub>	2.820	192	0	2.732	184	0
$\langle 4f^{13}5d(t_{2g})^1 \rangle$	2.796 ± 0.001	192 ± 1		2.703 ± 0.002	187 ± 1	
1 <sup>3</sup> T <sub>1u</sub>	2.799	193	2302	2.708	185	28 406
2 <sup>3</sup> T <sub>1u</sub>	2.797	192	5637	2.705	188	31 098
2 <sup>1</sup> T <sub>2u</sub>	2.795	192	9910	2.703	187	34 901
$\langle 4f^{13}5d(e_g)^1 \rangle$	2.840 ± 0.002	192 ± 1		2.743 ± 0.007	173 ± 4	
4 <sup>3</sup> T <sub>1u</sub>	2.841	194	19 854	2.750	176	48 013
3 <sup>3</sup> T <sub>2u</sub>	2.842	193	22 448	2.748	176	49 962
3 <sup>1</sup> T <sub>2u</sub>	2.841	193	23 831	2.745	174	50 962
5 <sup>3</sup> T <sub>1u</sub>	2.840	193	24 078	2.747	175	51 278
4 <sup>1</sup> T <sub>1u</sub>	2.839	191	26 486	2.724	176	51 567
4 <sup>3</sup> T <sub>2u</sub>	2.840	191	26 369	2.738	162	52 914
5 <sup>1</sup> T <sub>1u</sub>	2.834	191	30 225	2.743	172	53 010
3 <sup>1</sup> E <sub>u</sub>	2.840	192	24 809	2.749	176	53 071
3 <sup>3</sup> E <sub>u</sub>	2.840	192	24 358	2.749	176	53 163
4 <sup>1</sup> T <sub>2u</sub>	2.839	191	27 023	2.741	170	53 509
$\langle 4f^{13}6s^1 \rangle$	2.907 ± 0.001	203 ± 1		2.818 ± 0.001	175 ± 1	
6 <sup>3</sup> T <sub>1u</sub>	2.907	203	34 817	2.818	175	61 100
5 <sup>3</sup> T <sub>2u</sub>	2.907	203	35 124	2.819	176	61 308
2 <sup>3</sup> A <sub>2u</sub>	2.907	204	35 200	2.820	177	61 485
6 <sup>1</sup> T <sub>1u</sub>	2.906	204	35 583	2.816	173	61 983
2 <sup>1</sup> A <sub>2u</sub>	2.907	203	35 965	2.819	175	62 138
5 <sup>1</sup> T <sub>2u</sub>	2.906	203	35 869	2.818	174	62 195

<sup>a</sup> Yb–Br bond distances,  $R_e$ , in Å; totally symmetric vibrational frequencies,  $\bar{\nu}_{a_{1g}}$ , in cm<sup>-1</sup>; and minimum-to-minimum energy differences,  $T_e$ , relative to the 4f<sup>14</sup>–1<sup>1</sup>A<sub>1g</sub> ground state, in cm<sup>-1</sup>. Data for the 18 states in the 4f<sup>13</sup>5d(t<sub>2g</sub>)<sup>1</sup> manifold are given in ref 33; only those for the two lowest and the highest states are given here. Manifold averages and mean square deviations of the individual values with respect to the averages are labeled as  $\langle 4f^{13}5d(t_{2g})^1 \rangle$ ,  $\langle 4f^{13}5d(e_g)^1 \rangle$ , and  $\langle 4f^{13}6s^1 \rangle$ .

using the methods described in section II are presented in Tables 1 and 2 and Figures 1 and 2. They include the 4f<sup>14</sup> ground state and the electronic states showing main configurational character 4f<sup>13</sup>5d<sup>1</sup> and 4f<sup>13</sup>6s<sup>1</sup>.

The potential energy surfaces of all the states mentioned have been calculated first at the CASSCF(4f,5d,6s) level described in section II. Even though we refer to these states using simple labels corresponding to their main configuration, as above, the calculations are done in a space of about 10<sup>5</sup> configurations. Bonding interactions are only partially described, due to lack of dynamic correlation, nevertheless, the effects of the ligands and of the CsCaBr<sub>3</sub> host, modeled by the quantum mechanical AIMP embedding, are already visible and are responsible for the first energy gap observed, which splits the 4f<sup>13</sup>5d<sup>1</sup> manifold in two submanifolds, which can be called 4f<sup>13</sup>5d(t<sub>2g</sub>)<sup>1</sup> and 4f<sup>13</sup>5d(e<sub>g</sub>)<sup>1</sup>, and are formed, each, by parallel curves sharing bond distance and a<sub>1g</sub> vibrational frequency values. (As mentioned above, a detailed study of the 4f<sup>13</sup>5d(t<sub>2g</sub>)<sup>1</sup> manifold can be found in ref 33; for this reason, Tables 1 and 2 include only the data that are needed for this paper.) Whereas the bond lengths are shorter in the 4f<sup>13</sup>5d(t<sub>2g</sub>)<sup>1</sup> manifold than in the ground state, the opposite is true for the 4f<sup>13</sup>5d(e<sub>g</sub>)<sup>1</sup> states. These bond length differences have been observed before in f-element doped solids and have been analyzed in detail elsewhere.<sup>43,44</sup> In effect, on the basis of a quantum chemical analysis of interactions,<sup>43</sup> the bond length shifts have been interpreted as originating from two effects: (i) The inner f<sup>N</sup> open-shell is shielded by the outer p<sup>6</sup> closed-shell, whose interaction with the ligands dominates the bond length in the f<sup>N</sup> configuration, but the f → d excitation exposes the d electron to covalent interactions and leaves an inner f-hole behind, both effects leading to a shortening of the bond length upon excitation. (ii) A large effective ligand field, which is enhanced by covalency, stabilizes the d(t<sub>2g</sub>) and destabilizes the d(e<sub>g</sub>) molecular orbitals,

which further shortens the bond length in the f → d(t<sub>2g</sub>) excitation and lengthens it in the f → d(e<sub>g</sub>) excitation. All of these results show the much larger exposure of the 5d shell than the 4f shell to bonding and host interactions. The energy of the totally symmetric vibrational frequency,  $\bar{\nu}_{a_{1g}}$ , is basically the same for all states, at this level of calculation, regardless of their main configurational character.

As soon as dynamic correlation of all valence electrons is treated, using the MS-CASPT2 method referred in section II, the near degeneracy between the 4f<sup>14</sup> and 4f<sup>13</sup>5d(t<sub>2g</sub>)<sup>1</sup> shells is lifted and a large energy gap which separates the ground state from the first excited state is created (see Figure 1, right, and Table 1). Dynamic correlation is found to increase the 4f<sup>14</sup>–4f<sup>13</sup>5d(t<sub>2g</sub>)<sup>1</sup> and 4f<sup>14</sup>–4f<sup>13</sup>5d(e<sub>g</sub>)<sup>1</sup> energy differences by some 25 000 and 27 000 cm<sup>-1</sup>, respectively, on average, as can be seen in Table 1. The large transition energy corrections can be associated with the fact that electron correlation is much larger for tight 4f–4f electron pairs than for more distant 4f–5d electron pairs and the number of 4f–4f pairs substituted by 4f–5d pairs is largest in this 14f-electron system. Electron correlation is found to decrease all bond lengths significantly, by about 0.09–0.10 Å, the reduction being quite uniform; the  $\bar{\nu}_{a_{1g}}$  values are only slightly decreased.

Once scalar relativistic effects and dynamic electron correlation have been accounted for at the MS-CASPT2 level, it is possible to include spin–orbit coupling by doing spin–orbit CI calculations using the sfss Wood–Boring AIMP Hamiltonian, as described in section II. The effects of spin–orbit coupling become evident if the calculated potential energy surfaces of the 4f<sup>13</sup>5d(t<sub>2g</sub>)<sup>1</sup>, 4f<sup>13</sup>5d(e<sub>g</sub>)<sup>1</sup>, and 4f<sup>13</sup>6s<sup>1</sup> manifolds in Figure 2 are compared (see also Tables 1 and 2). New energy gaps are created which split the 4f<sup>13</sup>5d(t<sub>2g</sub>)<sup>1</sup>, 4f<sup>13</sup>5d(e<sub>g</sub>)<sup>1</sup> and 4f<sup>13</sup>6s<sup>1</sup> manifolds into two submanifolds each, which, using free ion language, correspond to the coupling of the 4f<sup>13</sup>(J = 7/2)

TABLE 2: Results of the Calculations on the (YbBr<sub>6</sub>)<sup>4-</sup> Cluster That Include CsCaBr<sub>3</sub> Embedding, 80 Valence Electron Correlation, and Relativistic Effects, up to Spin–Orbit Coupling<sup>a</sup>

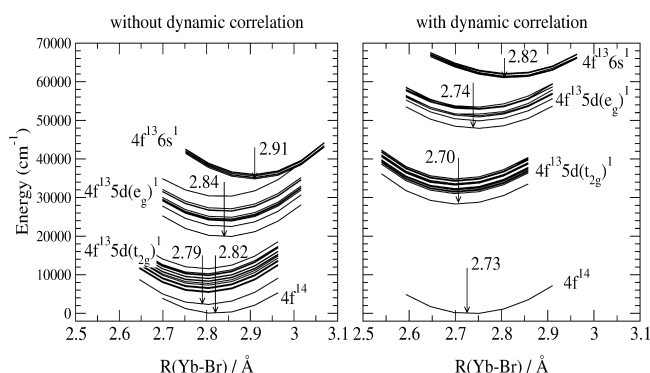
state <sup>b</sup>	<i>R</i> <sub>c</sub>	$\bar{\nu}_{\text{alg}}$	<i>T</i> <sub>c</sub>	<i>f</i> × 10 <sup>2</sup> <sup>c</sup>	weights of spin–orbit free wave functions <sup>d</sup>				
1 A <sub>1g</sub> ⟨4f <sup>13</sup> 5d(t <sub>2g</sub> ) <sup>1</sup> ⟩	2.732 2.704 ± 0.001	185 186 ± 2	0						
Lowest, Highest, and T <sub>1u</sub> States of the 4f <sup>13</sup> [7/2(2f)] × 5d(t <sub>2g</sub> ) <sup>1</sup> Submanifold <sup>b</sup>									
1 T <sub>2u</sub>	2.708	186	23 890		89.98	1 <sup>3</sup> T <sub>1u</sub>			
1 T <sub>1u</sub>	2.705	184	26 555	0.273	37.59	2 <sup>3</sup> T <sub>1u</sub>	33.99	1 <sup>1</sup> T <sub>1u</sub>	1 <sup>3</sup> E <sub>u</sub>
					9.49	1 <sup>3</sup> T <sub>1u</sub>			
2 T <sub>1u</sub>	2.705	184	26 598	1.260	32.20	1 <sup>3</sup> T <sub>1u</sub>	15.20	2 <sup>1</sup> T <sub>1u</sub>	1 <sup>3</sup> T <sub>2u</sub>
					11.76	2 <sup>3</sup> T <sub>1u</sub>	10.49	3 <sup>1</sup> T <sub>1u</sub>	1 <sup>1</sup> T <sub>1u</sub>
					5.66	3 <sup>3</sup> T <sub>1u</sub>			
3 T <sub>1u</sub>	2.705	187	27 200	0.030	45.13	1 <sup>3</sup> E <sub>u</sub>	24.15	2 <sup>3</sup> T <sub>1u</sub>	1 <sup>3</sup> T <sub>2u</sub>
					9.17	2 <sup>3</sup> T <sub>2u</sub>			
4 T <sub>1u</sub>	2.704	186	28 355	0.000	47.20	2 <sup>3</sup> E <sub>u</sub>	31.81	2 <sup>3</sup> T <sub>2u</sub>	1 <sup>1</sup> T <sub>1u</sub>
5 T <sub>1u</sub>	2.703	183	29 072	0.084	28.23	2 <sup>1</sup> T <sub>1u</sub>	21.17	2 <sup>3</sup> T <sub>2u</sub>	3 <sup>1</sup> T <sub>1u</sub>
					12.30	1 <sup>3</sup> T <sub>2u</sub>	8.18	1 <sup>3</sup> A <sub>1u</sub>	1 <sup>3</sup> T <sub>1u</sub>
6 T <sub>1u</sub>	2.703	186	29 884	0.489	43.21	3 <sup>3</sup> T <sub>1u</sub>	38.70	1 <sup>3</sup> A <sub>1u</sub>	
2 A <sub>2u</sub>	2.703	187	29 992		47.59	2 <sup>3</sup> T <sub>2u</sub>	45.80	1 <sup>1</sup> A <sub>2u</sub>	1 <sup>3</sup> T <sub>2u</sub>
Lowest, Highest, and T <sub>1u</sub> States of the 4f <sup>13</sup> [5/2(2f)] × 5d(t <sub>2g</sub> ) <sup>1</sup> Submanifold <sup>b</sup>									
3 A <sub>1u</sub>	2.707	186	34 560		93.95	1 <sup>3</sup> T <sub>1u</sub>			
7 T <sub>1u</sub>	2.707	182	35 916	1.524	40.38	1 <sup>3</sup> T <sub>1u</sub>	29.72	3 <sup>1</sup> T <sub>1u</sub>	1 <sup>3</sup> T <sub>2u</sub>
					8.84	1 <sup>3</sup> E <sub>u</sub>			
8 T <sub>1u</sub>	2.706	182	37 503	2.304	32.16	1 <sup>3</sup> T <sub>2u</sub>	21.80	2 <sup>1</sup> T <sub>1u</sub>	3 <sup>1</sup> T <sub>1u</sub>
					15.48	1 <sup>3</sup> E <sub>u</sub>			
9 T <sub>1u</sub>	2.703	184	38 301	0.033	37.78	1 <sup>1</sup> T <sub>1u</sub>	15.61	2 <sup>3</sup> T <sub>1u</sub>	1 <sup>3</sup> T <sub>2u</sub>
					11.15	1 <sup>3</sup> E <sub>u</sub>	10.78	2 <sup>3</sup> E <sub>u</sub>	
10 T <sub>1u</sub>	2.703	186	39 518	0.165	32.78	3 <sup>3</sup> T <sub>1u</sub>	22.81	2 <sup>3</sup> T <sub>2u</sub>	2 <sup>3</sup> E <sub>u</sub>
					14.99	1 <sup>3</sup> A <sub>1u</sub>			
11 T <sub>1u</sub>	2.703	184	39 830	0.021	28.49	1 <sup>3</sup> A <sub>1u</sub>	20.20	2 <sup>1</sup> T <sub>1u</sub>	2 <sup>3</sup> E <sub>u</sub>
					10.38	2 <sup>3</sup> T <sub>2u</sub>	9.25	3 <sup>1</sup> T <sub>1u</sub>	3 <sup>3</sup> T <sub>1u</sub>
⟨4f <sup>13</sup> 5d(e <sub>g</sub> ) <sup>1</sup> ⟩ <sup>c</sup>	2.745 ± 0.003	175 ± 4							
4f <sup>13</sup> [7/2(2f)] × 5d(e <sub>g</sub> ) <sup>1</sup> Submanifold									
8 E <sub>u</sub>	2.748	177	43 872		88.13	4 <sup>3</sup> T <sub>1u</sub>	9.72	3 <sup>3</sup> T <sub>2u</sub>	
11 T <sub>2u</sub>	2.748	177	43 912		88.30	4 <sup>3</sup> T <sub>1u</sub>	5.15	3 <sup>3</sup> T <sub>2u</sub>	
4 A <sub>2u</sub>	2.749	176	45 397		99.25	3 <sup>3</sup> T <sub>2u</sub>			
12 T <sub>2u</sub>	2.747	175	45 774		73.74	3 <sup>3</sup> T <sub>2u</sub>	22.78	3 <sup>1</sup> T <sub>2u</sub>	
12 T <sub>1u</sub>	2.745	175	46 445	4.227	29.60	5 <sup>3</sup> T <sub>1u</sub>	26.37	3 <sup>3</sup> T <sub>2u</sub>	4 <sup>3</sup> T <sub>1u</sub>
					12.95	5 <sup>1</sup> T <sub>1u</sub>			
5 A <sub>1u</sub>	2.747	175	46 664		96.60	5 <sup>3</sup> T <sub>1u</sub>			
13 T <sub>1u</sub>	2.743	181	46 937	2.400	41.98	5 <sup>3</sup> T <sub>1u</sub>	40.77	4 <sup>1</sup> T <sub>1u</sub>	3 <sup>3</sup> T <sub>2u</sub>
9 E <sub>u</sub>	2.747	175	47 152		36.56	5 <sup>3</sup> T <sub>1u</sub>	28.58	3 <sup>3</sup> T <sub>2u</sub>	3 <sup>1</sup> E <sub>u</sub>
13 T <sub>2u</sub>	2.747	175	47 460		35.18	5 <sup>3</sup> T <sub>1u</sub>	31.97	3 <sup>3</sup> E <sub>u</sub>	25.98
14 T <sub>1u</sub>	2.744	178	47 641	2.679	21.57	4 <sup>3</sup> T <sub>1u</sub>	20.81	3 <sup>3</sup> E <sub>u</sub>	5 <sup>1</sup> T <sub>1u</sub>
					12.39	4 <sup>1</sup> T <sub>1u</sub>	9.15	4 <sup>3</sup> T <sub>2u</sub>	5 <sup>3</sup> T <sub>1u</sub>
					6.00	3 <sup>3</sup> T <sub>2u</sub>			
10 E <sub>u</sub>	2.740	164	48 383		77.54	4 <sup>3</sup> T <sub>2u</sub>	17.72	3 <sup>1</sup> E <sub>u</sub>	
15 T <sub>1u</sub>	2.744	173	48 424	0.285	74.07	4 <sup>3</sup> T <sub>2u</sub>	20.69	3 <sup>3</sup> E <sub>u</sub>	
14T <sub>2u</sub>	2.743	172	48 619		49.26	4 <sup>1</sup> T <sub>2u</sub>	28.75	4 <sup>3</sup> T <sub>2u</sub>	12.70
					5.22	5 <sup>3</sup> T <sub>1u</sub>			3 <sup>3</sup> E <sub>u</sub>
Interacting 4f <sup>13</sup> [5/2(2f)] × 5d(e <sub>g</sub> ) <sup>1</sup> and 4f <sup>13</sup> [7/2(2f)] × 6s <sup>1</sup> Submanifolds									
6 A <sub>1u</sub>	2.749	176	53 859		96.53	4 <sup>3</sup> T <sub>1u</sub>			
16 T <sub>1u</sub>	2.743	161	55 345	4.950	45.77	4 <sup>3</sup> T <sub>1u</sub>	28.28	5 <sup>1</sup> T <sub>1u</sub>	3 <sup>3</sup> T <sub>2u</sub>
					6.92	3 <sup>3</sup> E <sub>u</sub>			
11 E <sub>u</sub>	2.739	195	56 062		57.43	3 <sup>3</sup> T <sub>2u</sub>	24.07	5 <sup>3</sup> T <sub>1u</sub>	3 <sup>1</sup> E <sub>u</sub>
					8.14	4 <sup>3</sup> T <sub>1u</sub>			
7 A <sub>1u</sub>	2.818	205	56 468		99.94	6 <sup>3</sup> T <sub>1u</sub>			
15 T <sub>2u</sub>	2.746	157	56 481		41.23	3 <sup>1</sup> T <sub>2u</sub>	20.79	5 <sup>3</sup> T <sub>1u</sub>	3 <sup>3</sup> T <sub>2u</sub>
					9.33	3 <sup>3</sup> E <sub>u</sub>	7.73	4 <sup>3</sup> T <sub>1u</sub>	
17 T <sub>1u</sub>	2.783	125	56 620	6.177	35.49	3 <sup>3</sup> T <sub>2u</sub>	24.69	4 <sup>1</sup> T <sub>1u</sub>	5 <sup>1</sup> T <sub>1u</sub>
					10.81	5 <sup>3</sup> T <sub>1u</sub>			
12 E <sub>u</sub>	2.803	260	56 801		44.13	3 <sup>1</sup> E <sub>u</sub>	36.67	5 <sup>3</sup> T <sub>1u</sub>	4 <sup>3</sup> T <sub>2u</sub>
18 T <sub>1u</sub>	2.804	190	57 024	1.230	66.58	6 <sup>3</sup> T <sub>1u</sub>	18.46	5 <sup>3</sup> T <sub>2u</sub>	3 <sup>3</sup> E <sub>u</sub>
16 T <sub>2u</sub>	2.816	162	57 159		42.74	3 <sup>3</sup> E <sub>u</sub>	34.93	5 <sup>3</sup> T <sub>1u</sub>	4 <sup>3</sup> T <sub>2u</sub>
5 A <sub>2u</sub>	2.827	170	57 293		96.16	4 <sup>3</sup> T <sub>2u</sub>			
17 T <sub>2u</sub>	2.799	239	57 355		48.41	5 <sup>3</sup> T <sub>2u</sub>	25.12	2 <sup>3</sup> A <sub>2u</sub>	6 <sup>3</sup> T <sub>1u</sub>
19 T <sub>1u</sub>	2.792	233	57 493	0.000	36.84	3 <sup>3</sup> E <sub>u</sub>	14.40	4 <sup>1</sup> T <sub>1u</sub>	4 <sup>3</sup> T <sub>2u</sub>
					9.92	5 <sup>1</sup> T <sub>1u</sub>	9.84	5 <sup>3</sup> T <sub>2u</sub>	5 <sup>3</sup> T <sub>1u</sub>
					6.05	6 <sup>3</sup> T <sub>1u</sub>			
13 E <sub>u</sub>	2.766	205	58 110		62.80	5 <sup>3</sup> T <sub>2u</sub>	36.62	6 <sup>3</sup> T <sub>1u</sub>	
18 T <sub>2u</sub>	2.761	223	58 154		29.27	5 <sup>1</sup> T <sub>2u</sub>	25.04	2 <sup>3</sup> A <sub>2u</sub>	4 <sup>3</sup> T <sub>2u</sub>
					13.59	4 <sup>1</sup> T <sub>2u</sub>	9.60	6 <sup>3</sup> T <sub>1u</sub>	
20 T <sub>1u</sub>	2.761	233	58 211	0.009	49.65	6 <sup>1</sup> T <sub>1u</sub>	36.97	5 <sup>3</sup> T <sub>2u</sub>	6 <sup>3</sup> T <sub>1u</sub>



TABLE 2: Continued

state <sup>b</sup>	$R_e$	$\bar{\nu}_{a_{1g}}$	$T_e$	$f \times 10^2$ <sup>c</sup>	weights of spin-orbit free wave functions <sup>d</sup>				
6 A <sub>2u</sub>	2.764	203	58 764	51.54	2 <sup>1</sup> A <sub>2u</sub>	45.05	5 <sup>3</sup> T <sub>2u</sub>		
19 T <sub>2u</sub>	2.755	214	58 932	32.22	4 <sup>3</sup> T <sub>2u</sub>	28.00	4 <sup>1</sup> T <sub>2u</sub>	19.08	5 <sup>1</sup> T <sub>2u</sub>
				9.72	6 <sup>3</sup> T <sub>1u</sub>	7.29	2 <sup>3</sup> A <sub>2u</sub>		
$\langle 4f^{13}6s^1 \rangle$	$2.819 \pm 0.001$	$177 \pm 3$							
4f <sup>13</sup> [5/2(2f)] × 6s <sup>1</sup> Submanifold									
14 E <sub>u</sub>	2.819	175	66 964	63.11	6 <sup>3</sup> T <sub>1u</sub>	36.84	5 <sup>3</sup> T <sub>2u</sub>		
20 T <sub>2u</sub>	2.819	177	67 051	46.52	6 <sup>3</sup> T <sub>1u</sub>	37.22	5 <sup>3</sup> T <sub>2u</sub>	11.18	2 <sup>3</sup> A <sub>2u</sub>
				5.02	5 <sup>1</sup> T <sub>2u</sub>				
21 T <sub>1u</sub>	2.818	174	67 353	0.027	6 <sup>1</sup> T <sub>1u</sub>	34.41	5 <sup>3</sup> T <sub>2u</sub>	19.68	6 <sup>3</sup> T <sub>1u</sub>
21 T <sub>2u</sub>	2.818	182	67 466		42.11	5 <sup>1</sup> T <sub>2u</sub>	31.30	2 <sup>3</sup> A <sub>2u</sub>	14.14
					12.40	5 <sup>3</sup> T <sub>2u</sub>			
7 A <sub>2u</sub>	2.819	175	67 473	53.40	5 <sup>3</sup> T <sub>2u</sub>	46.55	2 <sup>1</sup> A <sub>2u</sub>		

<sup>a</sup> Yb–Br bond distances,  $R_e$ , in Å; totally symmetric vibrational frequencies,  $\bar{\nu}_{a_{1g}}$ , in cm<sup>−1</sup>; minimum-to-minimum energy differences,  $T_e$ , relative to the 4f<sup>14</sup>–1A<sub>1g</sub> ground state, in cm<sup>−1</sup>; absorption oscillator strengths,  $f$ , and analyses of the spin-orbit wave functions. Manifold averages and mean square deviations of the individual values with respect to the averages are labeled as  $\langle 4f^{13}5d(t_{2g})^1 \rangle$ ,  $\langle 4f^{13}5d(e_g)^1 \rangle$ , and  $\langle 4f^{13}6s^1 \rangle$ . <sup>b</sup> Data for the 20 4f<sup>13</sup>[7/2(2F)] × 5d(t<sub>2g</sub>)<sup>1</sup> states and the 15 4f<sup>13</sup>[5/2(2F)] × 5d(t<sub>2g</sub>)<sup>1</sup> states are given in ref 33; only manifold averages and data relevant to this work are given here. <sup>c</sup> Oscillator strengths for the 1A<sub>1g</sub> → *i*T<sub>1u</sub> absorptions were calculated at the ground state equilibrium distance: 2.732 Å. <sup>d</sup> Weights (in %) larger than 5% are given. They have been calculated at  $R(\text{Yb–Br}) = 2.705$  Å. <sup>e</sup> Only states of the 4f<sup>13</sup>[7/2(2F)] × 5d(e<sub>g</sub>)<sup>1</sup> submanifold are included in the average. <sup>f</sup> Only states of the 4f<sup>13</sup>[5/2(2F)] × 6s<sup>1</sup> submanifold are included in the average.



**Figure 1.** Breathing mode potential energy curves of the 4f<sup>14</sup>, 4f<sup>13</sup>5d<sup>1</sup>, and 4f<sup>13</sup>6s<sup>1</sup> manifolds of CsCaBr<sub>3</sub>:(YbBr<sub>6</sub>)<sup>4−</sup>. All results include embedding and scalar relativistic effects. Left: spin-orbit free CASSCF(4f,5d,6s) calculations. Right: spin-orbit free MS-CASPT2-(Br48,Yb32) calculations. See text for details.

and 4f<sup>13</sup>(*J* = 5/2) subshell components with the 5d(t<sub>2g</sub>)<sup>1</sup>, 5d(e<sub>g</sub>)<sup>1</sup>, and 6s<sup>1</sup> electron, respectively. Due to the proximity in energy of the 4f<sup>13</sup>5d(e<sub>g</sub>)<sup>1</sup> and 4f<sup>13</sup>6s<sup>1</sup> manifolds, at the spin-orbit free level, on the one hand, and the magnitude of the 4f<sup>13</sup>(7/2) and 4f<sup>13</sup>(5/2) splitting, on the other hand (see below), the 4f<sup>13</sup>(5/2)5d(e<sub>g</sub>)<sup>1</sup> and 4f<sup>13</sup>(7/2)6s<sup>1</sup> submanifolds overlap in energy and significant 4f<sup>13</sup>5d(e<sub>g</sub>)<sup>1</sup> and 4f<sup>13</sup>6s<sup>1</sup> configuration interaction occurs between them. Since their average bond lengths are different ( $\langle R_e[4f^{13}5d(e_g)^1] \rangle = 2.74$  Å,  $\langle R_e[4f^{13}6s^1] \rangle = 2.82$  Å) the configurational mixing results in very distorted potential energy surfaces with intermediate bond length values (see Table 2). The spin-orbit splitting of the 4f<sup>13</sup> subshell can be estimated from the difference in the average energies of the 4f<sup>13</sup>(5/2)5d(t<sub>2g</sub>)<sup>1</sup> (38 100 cm<sup>−1</sup>) and 4f<sup>13</sup>(7/2)5d(t<sub>2g</sub>)<sup>1</sup> (27 600 cm<sup>−1</sup>) states, which is about 10 500 cm<sup>−1</sup> (Figure 2, right), or as the energy difference from the lowest states, which keep 4f<sup>13</sup>(5/2)5d(e<sub>g</sub>)<sup>1</sup> character, and the lowest states of the 4f<sup>13</sup>(7/2)5d(e<sub>g</sub>)<sup>1</sup> manifold, i.e.,  $T_e(6A_{1u}) - T_e(8E_u) = 10\,000$  cm<sup>−1</sup> (Table 2). These differences are close to the corresponding value in the free ion: 10 800 cm<sup>−1</sup>.<sup>45</sup>

A much smaller energy gap is found in the lower energy part of the 4f<sup>13</sup>(7/2)5d(t<sub>2g</sub>)<sup>1</sup> manifold, between states 1T<sub>2u</sub> and 1T<sub>1u</sub> (see Figure 2, right). This energy gap has been discussed in detail in ref 33, where it has been shown to be a consequence

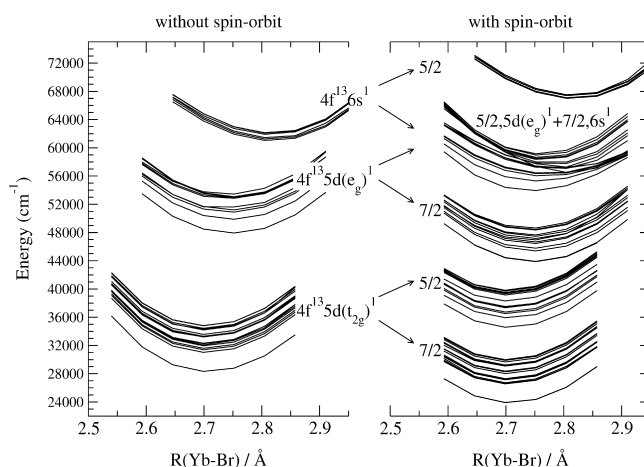


**Figure 2.** Breathing mode potential energy curves of the 4f<sup>13</sup>5d<sup>1</sup> and 4f<sup>13</sup>6s<sup>1</sup> manifolds of CsCaBr<sub>3</sub>:(YbBr<sub>6</sub>)<sup>4−</sup>. All results include embedding, scalar relativistic effects, and dynamic electron correlation of 80 valence electrons. Left: spin-orbit free MS-CASPT2-(Br48,Yb32) calculations. Right: spin-orbit CI calculations. Spin-orbit splitting of the manifolds in the left, leading to submanifolds in the right, is indicated with arrows. The submanifolds are labeled by the effective *J* value of their 4f<sup>13</sup> subshell. See text for details.

of the energy separation between the lowest high-spin state, 1<sup>3</sup>T<sub>1u</sub>, and the next higher 4f<sup>13</sup>5d(t<sub>2g</sub>)<sup>1</sup> state, as calculated at the spin-orbit free MS-CASPT2 level (see Figure 2, left).

**B. Absorption Spectrum of Yb<sup>2+</sup>-Doped CsCaBr<sub>3</sub>.** The envelope of the absorption spectrum presented in Figure 3 was produced as a superposition of the *a*<sub>1g</sub> vibrational progression of each individual electric dipole-allowed transitions 4f<sup>14</sup>–1A<sub>1g</sub> → *i*T<sub>1u</sub> (*i* = 1, 21) calculated using the semiclassical time-dependent approach of Heller with different values for the line broadening parameter (40 and 5 cm<sup>−1</sup> in the low- and high-resolution spectra, respectively).<sup>46–48</sup> To do this, the calculated equilibrium distance and *a*<sub>1g</sub> vibrational frequencies of the ground and excited states were used together with the corresponding minimum-to-minimum energy differences and absorption oscillator strengths (Table 2). Some electric dipole forbidden transitions that should be experimentally observable as low-intensity vibronic transitions preceding the intense electric dipole-allowed bands have been indicated with vertical bars.

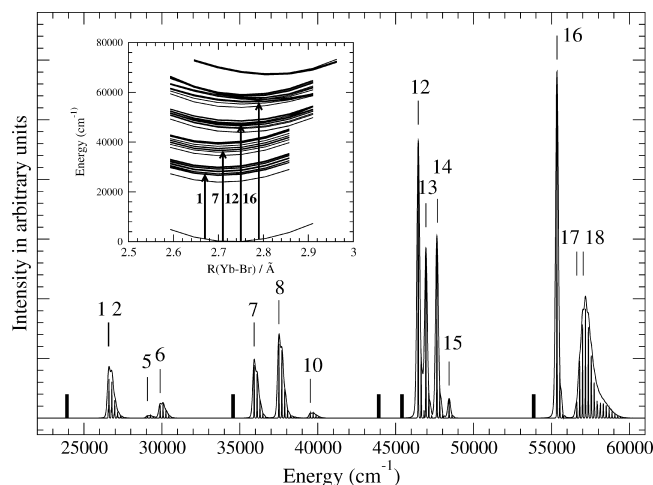


**Figure 3.** Calculated absorption spectrum of  $\text{CsCaBr}_3:(\text{YbBr}_6)^{4-}$  using spin-orbit CI data from Table 2 and different values for the line broadening parameter (40 and  $5 \text{ cm}^{-1}$  in the low- and high-resolution spectra, respectively). The 14 most intense  $T_{1u}$  electronic origins are indicated with the ordinals used in Table 2. Electric dipole forbidden transitions are indicated with vertical bars.

The calculated spectrum consists of four separated groups of bands (Figure 3). This structure is consistent with the existence of manifolds and submanifolds, separated by energy gaps, we have just discussed in subsection IIIA. The electronic origins with non-negligible absorption oscillator strengths that contribute to each group and their assignment to manifolds with a dominant configuration character are as follows: Group 1 is formed by origins  $i = 1, 2, 5$ , and  $6$  of manifold  $4f^{13}(7/2)5d(t_{2g})^1$ ; group 2, by origins  $i = 7, 8$ , and  $10$  of manifold  $4f^{13}(5/2)5d(t_{2g})^1$ ; group 3, by origins  $i = 12-15$  of manifold  $4f^{13}(7/2)5d(e_g)^1$ ; and group 4, by origins  $i = 16, 17$ , and  $18$ , of which, origin  $16T_{1u}$  has dominant  $4f^{13}(5/2)5d(e_g)^1$  character, whereas  $17T_{1u}$  and  $18T_{1u}$  have increasing  $4f^{13}6s^1$  contribution. In this way, whereas the crystal field effects on the  $5d$  electron are responsible for the energy difference between groups 1 and 3, on the one hand, and 2 and 4, on the other hand, the spin-orbit splitting of the  $4f^{13}$  subshell is responsible for the energy difference between groups 1 and 2 and, also, between groups 3 and 4.

The intensity of excitations to  $4f^{13}5d(t_{2g})^1$  states (groups 1 and 2) are significantly smaller than the intensity of excitations to  $4f^{13}5d(e_g)^1$  states (groups 3 and 4), by a factor of 3–4, as can be observed in Figure 3. This feature is related with atomic selection rules, as we comment next. On the one hand, the results presented in the previous subsection (Figure 2, Table 2) indicate that the 1, 2, and 3  $T_{1u}$  enabling terms of the spin-orbit free calculation contribute to the  $T_{1u}$  states of  $4f^{13}5d(t_{2g})^1$  character, whereas the terms 4 and 5  $T_{1u}$  contribute to those of  $4f^{13}5d(e_g)^1$  character. Furthermore, the calculated squares of the electric dipole transition moment,  $\mu^2$ , of pure spin-orbit free  $1^1A_{1g} \rightarrow i^1T_{1u}$  transitions, are 0.010, 0.186, 0.510, for  $i = 1, 2, 3$ , and 0.007 and 1.281, for  $i = 4, 5$ , which is consistent with the observation in Figure 3. On the other hand,  $\text{Yb}^{2+}$  free ion calculations performed by us using the same levels of methodology, reveal that the energy order of atomic  $4f^{13}5d^1$   $2S + 1 = 1$  terms, which lead to all 1 to  $5^1T_{1u}$  terms in the crystal, is as follows:  $^1H < ^1G < ^1F < ^1P$ . This makes it reasonable to expect that the  $^1P$  character is maximum for the highest  $4f^{13}5d^1$  crystal term,  $5^1T_{1u}$ . Hence, the large value of  $\mu^2(1^1A_{1g} \rightarrow 5^1T_{1u})$  and the observed higher intensity of excitations to  $4f^{13}5d(e_g)^1$  states can be related with atomic selection rules ( $\Delta L \pm 1$ ,  $\Delta S = 0$ ),

since the only atomic term leading to electric dipole-allowed transition in the  $4f^{13}5d^1$  manifold is  $^1P$ .

The vibrational progressions of the origins associated with the  $4f^{13}5d(t_{2g})^1$ ,  $4f^{13}5d(e_g)^1$ , and  $4f^{13}6s^1$  manifolds are also different and consistent with the absolute value of the offset of their characteristic bond length. The bond length differences relative to the ground state are  $\Delta R_e[4f^{13}5d(t_{2g})^1] = -0.029 \text{ \AA}$ ,  $\Delta R_e[4f^{13}5d(e_g)^1] = +0.011 \text{ \AA}$ , and  $\Delta R_e[4f^{13}6s^1] = +0.086 \text{ \AA}$ , at the MS-CASPT2 level (Table 1), and spin-orbit interaction changes these values only in the manifold of higher energy, where  $4f^{13}5d(e_g)^1$  and  $4f^{13}6s^1$  interaction occurs leading to intermediate values of equilibrium distances and offsets between  $+0.011$  and  $+0.086 \text{ \AA}$ . Hence, the vibrational progression intensities are as follows (see Figure 3 and confront individual equilibrium geometries in Table 2): For origins 1–10, of  $4f^{13}5d(t_{2g})^1$  character, the 0–0 and 0–1 lines have very similar and maximal intensity, and the progression includes up to the 0–3 member. For origins 12–15, of  $4f^{13}5d(e_g)^1$  character, the 0–0 line dominates the progression, which also includes, with much smaller intensity, the 0–1 member. Finally, the progressions of origins 16–18 show the effects of increasing mixing of  $4f^{13}5d(e_g)^1$  with  $4f^{13}6s^1$  configurations. So, the maximum intensity line moves from being the 0–0 (for origin 16) to the 0–3 (origin 17) to the 0–6 (for origin 18). Also, as the  $4f^{13}6s^1$  character becomes important (origin 18), the atomic selection rule that forbids  $f \leftrightarrow s$  transitions becomes apparent in the lower absorption oscillator strength value.

The fact that the  $4f^{13}6s^1$  states are so high in energy in the crystal, whereas they are among the lowest excited states in the free ion, is an interesting feature. The question of why these states are destabilized so strongly in the solid is discussed elsewhere.<sup>49</sup>

**C. Multiple Spontaneous Emissions in  $\text{CsCaBr}_3:\text{Yb}^{2+}$ .** In Table 3 we collect the data corresponding to the potentially emitting levels. They lie immediately above the five energy gaps we have just discussed and all but the highest in energy, which is probably in the conduction band (CB), should be stable enough to luminesce. To support this conclusion, we have estimated the approximate order,  $p$ , of the multiphonon process that could compete with the radiative emission from each level  $i\Gamma$ , as proposed in ref 10:  $p = E_{\text{gap}}(i\Gamma)/\hbar\nu_{\text{max}}$  (see Table 3). For this, we have used the energy gap below state  $i\Gamma$ ,  $E_{\text{gap}}(i\Gamma)$ , and the  $\bar{\nu}_{\text{ag}}$  value of the level lying below the gap as maximum phonon frequency,  $\nu_{\text{max}}$  (Table 2). The values of  $p$  make it reasonable to expect that multiphonon relaxation processes could be competitive in the case of the  $1T_{1u}$  state and negligible for the remaining states. The different spin character of the states lying above and below the gap also supports their stability, as revealed by the term analysis of the wave functions. Whereas the states lying above the large energy gaps,  $1T_{2u}$  (90%  $1^3T_{1u}$ ),  $1E_u$  (90%  $1^3T_{1u}$ ),  $3A_{1u}$  (94%  $1^3T_{1u}$ ),  $8E_u$  (88%  $4^3T_{1u}$ ), and  $6A_{1u}$  (97%  $4^3T_{1u}$ ), can be classified as high-spin states, since their spin-orbit wave functions are dominated by a particular high-spin term of  $T_{1u}$  spatial symmetry whose contribution is larger than 85%, the states lying below the large energy gaps show extensive spin-orbit mixing and cannot be classified as high-spin states nor as low-spin states, but as spin-mixed states. The opposite is true for the states lying above and below the smaller energy gap: whereas  $1T_{1u}$  and  $2T_{1u}$  (see Table 2), are spin-mixed states,  $1T_{2u}$  and  $1E_u$  are 90% high-spin  $1^3T_{1u}$ .

The characteristics of the predicted spontaneous emissions are summarized in Table 3; the two lowest emission bands are also presented in Figure 4. The first band is a double emission that corresponds to the  $1T_{2u}, 1E_u \rightarrow 1A_{1g}$  electric dipole

TABLE 3: Data of Potentially Emitting Levels and Characteristics of the Predicted Emissions<sup>a</sup>

	level	spin character	energy gap	$p^b$	emission characteristics	emission energy	
						calculated	observed <sup>c</sup>
4f <sup>13</sup> (7/2)5d(t <sub>2g</sub> ) <sup>1</sup>	1T <sub>2u</sub> , 1E <sub>u</sub>	high	23900	128	spin-forbidden, slow	23 900	23 000
	1T <sub>1u</sub> , 2T <sub>1u</sub>	mixed	2600	13	spin-enabled, 400 ns	26 600	24 500
4f <sup>13</sup> (5/2)5d(t <sub>2g</sub> ) <sup>1</sup>	3A <sub>1u</sub>	high	4600	24	spin-forbidden, slow	34 600	
4f <sup>13</sup> (7/2)5d(e <sub>g</sub> ) <sup>1</sup>	8E <sub>u</sub>	high	4000	22	spin-forbidden, slow	43 900	
4f <sup>13</sup> (5/2)5d(e <sub>g</sub> ) <sup>1</sup>	6A <sub>1u</sub>	high	5200	30	not observable (in CB)	53 900	

<sup>a</sup> Energies are given in cm<sup>-1</sup>. <sup>b</sup> Multiphonon order,  $p = E_{\text{gap}}(i\Gamma)/\hbar\nu_{\text{max}}$ . See text for details. <sup>c</sup> Peak position approximately read from the 77 K emission spectrum of ref 3.

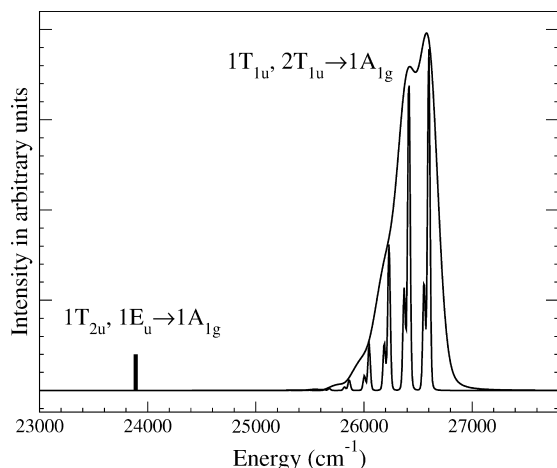


**Figure 4.** First two bands of the calculated emission spectrum of CsCaBr<sub>3</sub>:(YbBr<sub>6</sub>)<sup>4-</sup> using spin-orbit CI data from Table 2 and different values for the line broadening parameter (40 and 5 cm<sup>-1</sup> in the low- and high-resolution spectra, respectively). The electric dipole forbidden emissions are indicated with vertical bars.

forbidden transitions and is indicated with vertical bars in Figure 4. As mentioned above, it can be labeled as a spin-forbidden band and it should lead to a slow emission. The second band is an electric dipole-allowed double emission and its envelope has been calculated as a superposition of the a<sub>1g</sub> vibrational progression of the individual electric dipole-allowed transitions 1T<sub>1u</sub>, 2T<sub>1u</sub> → 1A<sub>1g</sub> using the semiclassical time-dependent approach of Heller.<sup>46–48</sup> Their emission oscillator strengths [ $f(1T_{1u} \rightarrow 1A_{1g}) = -0.273 \times 10^{-2}$ ,  $f(2T_{1u} \rightarrow 1A_{1g}) = -1.260 \times 10^{-2}$ ] and spectroscopic data in Table 2 have been used for that purpose, and thermal equilibrium among 1T<sub>1u</sub> and 2T<sub>1u</sub> has been assumed, so that the contribution of the progression of the latter has been scaled by the corresponding Boltzmann factor (0.45 for T = 77 K). As commented above, the emitting states in this band are spin-mixed and this band drives its intensity from no other terms than the enabling low-spin <sup>1</sup>T<sub>1u</sub> states that contribute to their spin-orbit wave functions; for this reason, this band has been called “spin-enabled” in ref 33, where a detailed study of the differences in the electronic structure of the low-lying excited states of CsCaBr<sub>3</sub>:Yb<sup>2+</sup> has been presented. The spontaneous emission from these states should be significantly faster. The calculated emission lifetimes of 1T<sub>1u</sub> and 2T<sub>1u</sub> are respectively 1100 and 150 ns; when thermal equilibrium is considered, the band emission lifetime becomes 400 ns. Finally, the third and fourth emission bands, corresponding to 3A<sub>1u</sub> → 1A<sub>1g</sub> and 8E<sub>u</sub> → 1A<sub>1g</sub>, respectively, are also electric dipole forbidden, spin-forbidden, slow emissions, as indicated in Table 3.

**D. Theory and Experiment.** Heavy Ln<sup>3+</sup> and Ln<sup>2+</sup> ions in crystals share the following interesting spectral features: (representative references are refs 2, 4, 9, 14, and 50): (i) A weak band is present in their f–d absorption and/or excitation spectra

at lower energies than the strong f–d bands. (ii) A slow d–f emission band is observed in their luminescence spectra at lower energies than a fast d–f emission band (the emissions referred to are to the 4f<sup>N</sup> ground state). (iii) Strong temperature dependence of the relative intensities of these emissions has been reported and it has been interpreted as a manifestation of competing radiative and nonradiative decay from the higher state, which favors nonradiative feeding of the lower state as the rate of the nonradiative process increases with temperature, so that a gradual change of relative intensities is observed from the low-T limit, where the intensity of the higher, fast emission is largest, to the high-T limit, where the intensity of the lower, slow emission is largest.

The first two bands of the calculated absorption and emission spectra of CsCaBr<sub>3</sub>:Yb<sup>2+</sup>, presented here, agree with (i) and (ii), respectively. The prediction that nonradiative decay from 1T<sub>1u</sub> and 2T<sub>1u</sub> to 1T<sub>2u</sub> and 1E<sub>u</sub> should be competitive with radiative decay, discussed above, is also in agreement with (iii). However, the methods used here do not allow us to calculate nonradiative relaxation rates and, hence, the temperature dependence of the relative intensity of the first two emission bands cannot be calculated; furthermore, the spontaneous emission lifetime calculated here refers only to the radiative process (which, nevertheless, is useful to infer the contribution of the nonradiative process to the experimental emission lifetime). Taking all of the latter into account, the calculated emission lifetime and emission spectrum in Figure 4 should be comparable with the low-T emission lifetime and emission spectrum. As far as we know, the only report on the spectral features of CsCaBr<sub>3</sub>:Yb<sup>2+</sup> crystals is that of ref 3. The 77 and 300 K emission spectra were presented in the range 21 000–25 800 cm<sup>-1</sup>. Both spectra show two very broad, structureless bands whose relative intensities vary with temperature, as we have just described. The peak positions at 77 K seem to be at 23 000 and 24 500 cm<sup>-1</sup>, the intensity of the lower band is almost negligible, and no report on emission lifetime values was given. Our results agree with the intensity pattern, deviate 900 and 2100 cm<sup>-1</sup> from the peak positions (Table 3), give a 20% narrower higher band, and a too large (by 900 cm<sup>-1</sup>, 50%) gap between the two bands.

The comparison with the data reported in ref 3 is, however, very uncertain and more experimental work is necessary which explores lower temperatures and emission lifetimes, and, very important, which extends the investigation of the emission spectrum to much higher energies, given the predictions of this paper on multiple luminescence.

#### IV. Conclusions

Multiple spontaneous 4f<sup>13</sup>5d<sup>1</sup> → 4f<sup>14</sup> emissions are predicted in Yb<sup>2+</sup>-doped CsCaBr<sub>3</sub> crystals by ab initio quantum chemical calculations. Four emission bands are found at 23 900, 26 600, 34 600, and 43 900 cm<sup>-1</sup> that should be experimentally observ-



able at low temperatures. They are assigned to emissions from the following electronic states, respectively:  $4f^{13}(7/2)5d(t_{2g})^1-1T_{2u}$ ,  $1E_u$ ;  $4f^{13}(7/2)5d(t_{2g})^1-1T_{1u}$ ,  $2T_{1u}$ ;  $4f^{13}(5/2)5d(t_{2g})^1-3A_{1u}$ ;  $4f^{13}(7/2)5d(e_g)^1-8E_u$ . The first, third, and fourth bands are slow, electric dipole forbidden emissions, which can be described as spin-forbidden given that the corresponding spin-orbit wave functions are dominated (88–97%) by a single term of  $^3T_{1u}$  symmetry. The second band is a fast, electric dipole-allowed emission that cannot be described as spin-allowed, because it is an extensive mixture of terms; rather, it can be described as spin-enabled, because it gets its intensity from the contributions of  $^1T_{1u}$  enabling terms; its spontaneous (radiative) emission lifetime is 400 ns. Large energy gaps are found below the emitting levels of the slow bands (23 900, 4600, 4000  $\text{cm}^{-1}$ , respectively), relative to the maximum local phonon energies calculated (around 185  $\text{cm}^{-1}$ ), which indicates that these states should be significantly stable and multiphonon relaxation to the lower states should be negligible. A smaller gap is found below the states of the fast band (2600  $\text{cm}^{-1}$ ), which should result in a temperature dependent competition between radiative and multiphonon decay. Differential correlation between  $4f-4f$  and  $4f-5d$  pairs (which increases the energy differences by 25 000–27 000  $\text{cm}^{-1}$ ), splitting of the  $5d$  shell by interactions with the host (around 19 000–20 000  $\text{cm}^{-1}$ ), and spin-orbit effects within the  $4f^{13}$  subshell (which is found to be about 10500  $\text{cm}^{-1}$ ) contribute to the existence of five energy gaps in the  $4f^{13}5d^1$  and  $4f^{13}6s^1$  manifolds that split the absorption spectrum into four groups of separate bands, three of which could lie below the host absorption, and are the bases for the predicted multiple emissions. The quantum chemical methods employed make use of explicit wave functions expanded in terms of flexible basis sets (of triple- $\zeta$  plus polarization quality, plus diffuse functions for anions), multireference spaces and multireference second-order perturbation methods (MS-CASPT2) to account for nondynamic and dynamic correlation, scalar and relativistic terms in the  $(\text{YbBr}_6)^{4-}$  cluster Hamiltonian (spin-free-state-shifting Wood–Boring AIMP), and quantum mechanical embedding potentials (AIMP embedding) to represent the host crystal. Typical discrepancies with experimental transition energies obtained in previous applications to similar systems using the same combination of methods make it reasonable to expect overestimations lower than 10%; this suggests that the predicted transition energies could be observed experimentally some 2000–3000  $\text{cm}^{-1}$  below the predicted values.

**Acknowledgment.** This research was supported in part by Ministerio de Ciencia e Innovación, Spain, under contracts CTQ2005-08550 and MAT2008-05379. G.S–S. acknowledges an FPI fellowship from Ministerio de Ciencia e Innovación, Spain.

## References and Notes

- Rubio, J. J. *Phys. Chem. Solids* **1991**, 52, 101.
- Pan, Z.; Duan, C.; Tanner, P. A. *Phys. Rev. B* **2008**, 77, 085114.
- Larsen, P.; Adlung, M.; Wickleder, C. Rare Earth Conference, Wrocław, 2006 (unpublished), Abstract CI3.
- Grimm, J.; Güdel, H. U. *Chem. Phys. Lett.* **2005**, 404, 40.
- Grimm, J.; Wenger, O. S.; Krämer, K. W.; Güdel, H. U. *J. Lumin.* **2007**, 126, 590.
- Beurer, E.; Grimm, J.; Gerner, P.; Güdel, H. U. *J. Am. Chem. Soc.* **2006**, 128, 3110.
- Grimm, J.; Beurer, E.; Gerner, P.; Güdel, H. U. *Chem.–Eur. J.* **2007**, 13, 1152.
- Kück, S. *Appl. Phys. B: Laser Opt.* **2001**, 72, 515.
- Grimm, J.; Beurer, E.; Güdel, H. U. *Inorg. Chem.* **2006**, 45, 10905.
- Riseberg, L. A.; Moos, H. W. *Phys. Rev.* **1968**, 174, 429.
- Moos, H. W. *J. Lumin.* **1970**, 2 (1), 106.
- Struck, C. W.; Fonger, W. H. *J. Lumin.* **1975**, 10, 1.
- Reber, C.; Güdel, H. U. *J. Lumin.* **1990**, 47, 7.
- Wegh, R. T.; Meijerink, A. *Phys. Rev. B* **1999**, 60, 10820.
- Roos, B. O.; Taylor, P. R.; Siegbahn, P. E. M. *Chem. Phys.* **1980**, 48, 157.
- Siegbahn, P. E. M.; Heiberg, A.; Almlöf, J.; Roos, B. O. *J. Chem. Phys.* **1981**, 74, 2384.
- Siegbahn, P.; Heiberg, A.; Roos, B.; Levy, B. *Phys. Scr.* **1980**, 21, 323.
- Andersson, K.; Malmqvist, P.-Å.; Roos, B. O.; Sadlej, A. J.; Wolinski, K. *J. Phys. Chem.* **1990**, 94, 5483.
- Andersson, K.; Malmqvist, P.-Å.; Roos, B. O. *J. Chem. Phys.* **1992**, 96, 1218.
- Seijo, L.; Barandiarán, Z. In *Computational Chemistry: Reviews of Current Trends*; Leszczyński, J., Ed.; World Scientific: Singapore, 1999; Vol. 4, p 55.
- Huang, P.; Carter, E. A. *Annu. Rev. Phys. Chem.* **2008**, 59, 261.
- Seijo, L.; Barandiarán, Z. In *Relativistic Electronic Structure Theory: Part 2. Applications*; Schwerdtfeger, P., Ed.; Elsevier: Amsterdam, 2004; pp 417–475.
- Tanner, P. A.; Mak, C. S. K.; Edelstein, N. M.; Murdoch, K. M.; Liu, G.; Huang, J.; Seijo, L.; Barandiarán, Z. *J. Am. Chem. Soc.* **2003**, 125, 13225.
- Ruipérez, F.; Seijo, L.; Barandiarán, Z. *J. Chem. Phys.* **2005**, 122, 234507.
- Gracia, J.; Seijo, L.; Barandiarán, Z.; Curulla, D.; Niemansverdriet, H.; van Gennip, W. J. *Lumin.* **2008**, 128, 1248.
- Zaitsevskii, A.; Malrieu, J. P. *Chem. Phys. Lett.* **1995**, 233, 597.
- Finley, J.; Malmqvist, P.-Å.; Roos, B. O.; Serrano-Andrés, L. *Chem. Phys. Lett.* **1998**, 288, 299.
- Seijo, L. *J. Chem. Phys.* **1995**, 102, 8078.
- Barandiarán, Z.; Seijo, L. *J. Chem. Phys.* **1988**, 89, 5739.
- Seijo, L.; Barandiarán, Z.; Ordejón, B. *Mol. Phys.* **2003**, 101, 73.
- Barandiarán, Z.; Seijo, L. *Can. J. Chem.* **1992**, 70, 409.
- Seijo, L.; Barandiarán, Z.; Harguindey, E. *J. Chem. Phys.* **2001**, 114, 118.
- Andzelm, J.; Klobukowski, M.; Radzio-Andzelm, E.; Sakai, Y.; Tatewaki, H. In *Gaussian Basis Sets for Molecular Calculations*; Huzinaga, S., Ed.; Elsevier: Amsterdam, 1984.
- From B. Roos unpublished ANO-RCC basis set for Br included in the MOLCAS basis set libraries.
- Sánchez-Sanz, G.; Seijo, L.; Barandiarán, Z. *J. Chem. Phys.* **2009**, 131, 024505.
- Seifert, H. J.; Haberhauer, D. Z. *Anorg. Allg. Chem.* **1982**, 491, 301.
- Evjen, H. M. *Phys. Rev.* **1932**, 39, 675.
- Seijo, L.; Barandiarán, Z. *J. Chem. Phys.* **2003**, 118, 5335.
- Karlström, G.; Lindh, R.; Malmqvist, P. A.; Roos, B. O.; Ryde, U.; Veryazov, V.; Widmark, P. O.; Cossi, M.; Schimmelpfennig, B.; Neogrady, P.; Seijo, L. *Comput. Mater. Sci.* **2003**, 28, 22.
- Barandiarán, Z.; Seijo, L. *J. Chem. Phys.* **2003**, 118, 7439.
- Llugar, R.; Casarrubios, M.; Barandiarán, Z.; Seijo, L. *J. Chem. Phys.* **1996**, 105, 5321.
- COLUMBUS suite of programs. (ARGOS, CNVRT, SCFPQ, LSTRN, CGDBG, and CIDBG.) R. M. Pitzer (principal author). See: Chang, A. H. H.; Pitzer, R. M. *J. Am. Chem. Soc.* **1989**, 111, 2500, and references therein for a description. CNVRT and LSTRN have been adapted to handle AIMP integrals by L. Seijo. CIDBG has been modified for spin-free-state-shifted spin-orbit CI calculations by M. Casarrubios.
- Vallet, V.; Maron, L.; Teichteil, C.; Flament, J.-P. *J. Chem. Phys.* **2000**, 113, 1391.
- Detailed core and embedding AIMP data libraries in electronic format are available from the authors upon request or directly at the address <http://www.uam.es/quimica/aimp/Data/AIMPLibs.html>. See also ref 37.
- Barandiarán, Z.; Seijo, L. *J. Chem. Phys.* **2003**, 119, 3785.
- Barandiarán, Z.; Edelstein, N. M.; Ordejón, B.; Ruipérez, F.; Seijo, L. *J. Solid State Chem.* **2005**, 178, 464.
- Bryant, B. W. *J. Opt. Soc. Am.* **1965**, 55, 771.
- Heller, E. J. *J. Chem. Phys.* **1975**, 62, 1544.
- Heller, E. J. *Acc. Chem. Res.* **1981**, 14, 368.
- Zink, J. I.; Shin, K. S. *Molecular distortions in excited electronic states determined from electronic and resonance raman spectroscopy*; Advances in Photochemistry; Wiley: New York, 1991; Vol. 16, pp 119–214.
- Sánchez-Sanz, G.; Seijo, L.; Barandiarán, Z. *Spectrosc. Lett.*, in press.
- van Pieterse, L.; Reid, M. F.; Burdick, G. W.; Meijerink, A. *Phys. Rev. B* **2002**, 65, 045114.